

pubs.acs.org/JPCC Article

Symmetry-Dependent Dynamics in Au₃₈(SC₆H₁₃)₂₄ Revealed by Polarization-Dependent Two-Dimensional Electronic Spectroscopy

William R. Jeffries, Christine M. Aikens,* and Kenneth L. Knappenberger, Jr.*



Cite This: J. Phys. Chem. C 2023, 127, 19035–19043



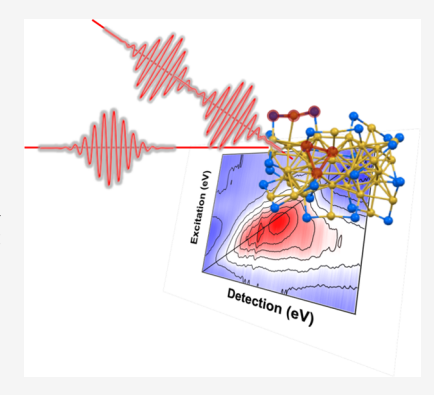
ACCESS I

III Metrics & More

Article Recommendations

Supporting Information

ABSTRACT: Structurally precise metal nanoclusters exhibit complex electronic relaxation dynamics that differ from those of plasmonic nanoparticles. Here, we show the importance of the electronic state symmetry in determining the relaxation pathways of gold nanoclusters. Polarization-dependent two-dimensional (2D) electronic spectroscopy (p-2DES) was used to map state-specific relaxation dynamics in $Au_{38}(SC_6H_{13})_{24}$ monolayer-protected clusters (MPCs). A positive-amplitude differential signal at 1.96 eV excitation and detection energies that spanned 1.91–2.05 eV was resolved in the p-2DES cross-peak specific spectra. The positive-amplitude signal stood out from the otherwise broad transient bleach signals due to its unique time-dependent amplitude, anisotropy, and transition orientation angles. Density functional theory (DFT) calculations and selection rules indicated that the positive-amplitude signal in $S_{\rm cp}$ spectra feature most likely corresponds to a dark E-symmetry state localized to the MPC Au–S ligand band. Time-dependent analysis of p-2DES-detected cross-peaks at different excitation-detection energies indicated that the



dark state is indirectly populated through relaxation of the initially excited bright states and relaxes through a pathway that is uniquely accessed by 1.96 eV excitation. These results reveal the surprising influence of excited state symmetry on carrier relaxation for metal colloids in the range of 1–2 nm, where electronic state densities are high. These insights are made possible by the combined use of p-2DES and DFT, which made state assignments possible. State-selective dynamics may provide a strategy for controlling the energy flow in metal nanoclusters.

INTRODUCTION

Quantum confinement leads to a variety of interesting electronic dynamics and optical properties in colloidal nanoparticles. Photoexcitation of gold nanoparticles typically results in successive ultrafast electron-electron scattering, picosecond electron-phonon coupling, and subsequent energy dissipation to the surroundings. These rates can be affected by the spatial confinement of the metal colloids. For example, gold nanospheres exhibit size-dependent collective electronphonon coupling that increases from a few hundred femtoseconds to a few picoseconds for particle diameters between 2 and 8 nm. For metal nanoclusters in the 1-2 nm range, a few reports have demonstrated evidence of electronic-state-specific carrier relaxation mechanisms.³⁻⁷ In particular, ultrafast twodimensional electronic spectroscopy (2DES) has been used to resolve carrier dynamics in the superatomic P and D states in $Au_{25}(SC_8H_9)_{18}$ monolayer-protected clusters (MPCs).⁷ In addition to electronic structure, geometric structure determines picosecond metal-to-ligand charge transfer processes for metal nanoclusters of the sub-2 nm size.⁸ The large influence of both electronic state and geometric structural specificity in metal nanocluster dynamics is surprising given the high density of states for these systems. An important area that has not been addressed for these gold domains is understanding the influence of the electronic state symmetry in governing relaxation dynamics in colloidal metals.

MPCs are structurally well-defined colloidal nanoscale metals. Generally, thiol-protected MPCs are well described by three structural motifs: (i) an all-metal gold kernel; (ii) an inorganic semiring that consists of alternating Au-S staple-like units that form the ligand band; and (iii) surface passivating organothiolate ligands (SR) that provide colloidal stability. 9,10 Synthetic control of MPC structure has been leveraged to influence optical properties like spin-polarized and size-scalable photoluminescence. 11-13 Metal clusters, including MPCs, also serve as a bridge for describing mechanisms of metal-based catalysis that in part, derive their functional responses from size, geometry, and composition-dependent electronic properties of the system. 14-18 Hence, MPCs provide a platform for achieving structural control over energy relaxation mechanisms on nanoscale metals. Although MPCs are structurally well defined, they exhibit a high density of states and complex dynamics. Therefore, understanding energy flow in MPCs is an integral step toward the targeted development of metal-based

Received: July 18, 2023
Revised: September 3, 2023
Published: September 14, 2023





photonic and quantum information technologies and larger cluster-assembled materials.

Of the numerous isolated MPCs, $Au_{38}(SR)_{24}$ is of particular interest because it is characterized by a variety of metalcentered and metal-to-ligand charge transfer transitions spanning the visible and near-infrared frequencies but is small enough to afford reliable theoretical descriptions of electronic excitation spectra. 19-21 Neutral Au₃₈(SR)₂₄ MPCs were first structurally characterized at the single-crystal level by Jin et al. in $2010.^{22}$ The $Au_{38}(SR)_{24}$ kernel consists of a 23gold-atom bi-icosahedral structure that is surrounded by six Au₂(SR)₃ dimeric and three Au(SR)₂ monomeric staple-like motifs that are passivated by 24 surface ligands. Timedependent density functional theory (TDDFT) calculations have been used to characterize the many metal-centered and ligand-to-metal charge transfer (LMCT) transitions of $Au_{38}(SR)_{24}$. This includes the greatest oscillator strength transition, with its largest weight from the LUMO ← HOMO - 8 transition that originates from excitations out of the semiring and additionally involves several metal-centered transitions that predominantly originate from the all-metal kernel.^{20,21} (It should be noted that some references denote a degenerate orbital as a single orbital (such as HOMO - 8), whereas other references examine splitting of degeneracies and thus use two different orbital designations (such as HOMO -12/HOMO - 13) for the corresponding set of orbitals; orbital information for Au₃₈(SH)₂₄ at the PBE/TZP level of theory is provided in Table S1.) The mixed nature of the charge transfer resonance in Au₃₈(SR)₂₄ MPCs makes it a model system to investigate state-specific electronic relaxation dynamics in quantum-confined metals and technologically relevant metalchalcogenide interfaces.

Two-dimensional electronic spectroscopy (2DES) has been used to obtain insights on state-specific relaxation dynamics in several biological, 23,24 molecular, 25,26 and nanomaterial systems. 27-30 In time-resolved 2DES, Fourier transformation of the transient signal collected as a function of the time delay between two phase-locked excitation pulses provides an excitation-energy axis that is used to map the initial electronic excitation of the system to its detected time-dependent thirdorder response, yielding a frequency-frequency correlation that reports on coupling of excited states and thermalization processes via line shape and amplitude modulations.31,32 Recently, our group used 2DES to study ultrafast carrier relaxation through the manifold of charge transfer resonances in neutral Au₃₈(SC₆H₁₃)₂₄.⁶ It was determined that (i) excitation is dominated by the higher-lying LUMO ← HOMO - 8 transition; (ii) charge carriers relax through internal conversion into a manifold (LUMO \leftarrow HOMO - n) of mixed, inorganic semiring and metal kernel states within 150 fs; and (iii) carriers relax through a picosecond charge transfer process prior to radiative recombination in the kernel-localized LUMO ← HOMO manifold. However, the high density of electronic states limited the identification of specific states that govern relaxation.

Here, we discuss the use of polarization-selective 2DES (p-2DES) to distinguish the influence of excited state symmetry on carrier relaxation dynamics in Au₃₈(SC₆H₁₃)₂₄. p-2DES allows isolation of specific signals of interest through use of coand cross-pump and probe polarization vectors³³ and has enabled assignment of state-specific dynamics in cadmium selenide quantum dots, ³⁴ gallium arsenide quantum wells, ³⁵ carbon nanotubes, ³⁶ and photosynthetic complexes. ^{37,38} Here,

p-2DES was used in the partially collinear geometry to suppress strong on-diagonal signals and isolate off-diagonal cross-peaks. We resolved a low-amplitude positive-polarity signal that was indirectly populated following 1.96 eV excitation and is assigned to the Au-S semiring transition (LUMO \leftarrow HOMO - 7) of E symmetry. This specific E symmetry transition is unique among other E states, which predominantly originate from excitations out of the all-metal kernel. Analysis of the time dependence of p-2DES cross-peaks indicated that the unique E state was indirectly populated by relaxation of the initially excited manifold of bright states that made up the charge transfer transition. The E-symmetry species also relaxed through a mechanism different from the majority of excited charge transfer states. These results suggest that despite having a large density of nearly degenerate states, state specificity and symmetry are important factors for determining carrier relaxation dynamics in Au₃₈(SC₆H₁₃)₂₄. These results also highlight the complex interplay between nanocluster structural domains and carrier relaxation dynamics in small 1-2 nm sized MPCs.

EXPERIMENTAL METHODS

Synthesis of Au₃₈(SC₆H₁₃)₂₄ Monolayer-Protected Clusters. Synthesis was carried out following a previously published protocol.³⁹ The two-step synthesis was carried out as follows: first, water-soluble L-glutathione-protected clusters were synthesized through a combination of tetrachloroauric acid trihydrate and L-glutathione (SG) dissolved in methanol and distilled water, respectively. The solution was stirred for 15 min at 0 °C, which resulted in a yellow-brown suspension. Dissolved clusters were reduced by adding a sodium borohydride solution in water, immediately turning the solution black. The solution was then stirred for 60 min. The Au_n(SG)_m clusters were resuspended in a 1:1 water/ acetone mixture and combined with hexanethiol and then stirred at 80 °C for 3 h. Finally, the organic phase, which contained $Au_{38}(SC_6H_{13})_{24}$ nanoclusters, was washed with methanol to remove excess ligands, and the nanoclusters were dissolved in toluene for ultrafast experiments. No additional separation was required.

Two-Dimensional Electronic Spectroscopy. Experimental details of the femtosecond 2DES setup have been described previously. 6,40,41 A brief description is included here. Fundamental seed pulses at 1040 nm from a solid-state ytterbium amplifier (Spirit; Spectra-Physics) were modulated to a 100 kHz repetition rate and used to seed a dual-stage noncollinear optical parametric amplifier (NOPA). The NOPA was used to generate visible pump and probe pulses centered at 630 nm with a full width at half-maximum (fwhm) of 33 nm, which were compressed after frequency mixing. The pulses were sent to a pulse-shaper-based 2DES QuickVisible setup (PhaseTech). Pump and probe pulses were generated and separated using a 90/10 (pump/probe) beam splitter. The pump beam was focused and spatially overlapped with the probe pulse at the sample after being temporally delayed by using a mechanical delay stage. For 2DES measurements, the pump was dispersed and collimated using a two-grating twoparabolic mirror pair before being guided into an acousto-optic modulator (AOM), which was used to generate the two phaselocked pump-pulse pair with a controlled time delay (t_1) . A half-wave plate/polarizer was used to set the pump beam to the co- and cross-polarized configuration. The pump pulses were temporally delayed using a mechanical delay stage to generate

the pump–probe waiting time $(T_{\rm w})$. The transmitted probe was dispersed and self-heterodyne detected using an SP2150i array detector (Princeton Instruments). The ultrafast 2DES measurements were conducted in the partially collinear pump–probe geometry, yielding the absorptive 2DES spectra.

RESULTS AND DISCUSSION

Consistent with the previously reported $Au_{38}Q$ isomer, the calculated geometries of the metal kernel and inorganic semiring structures of $Au_{38}(SH)_{24}$ are shown in Figure 1a.

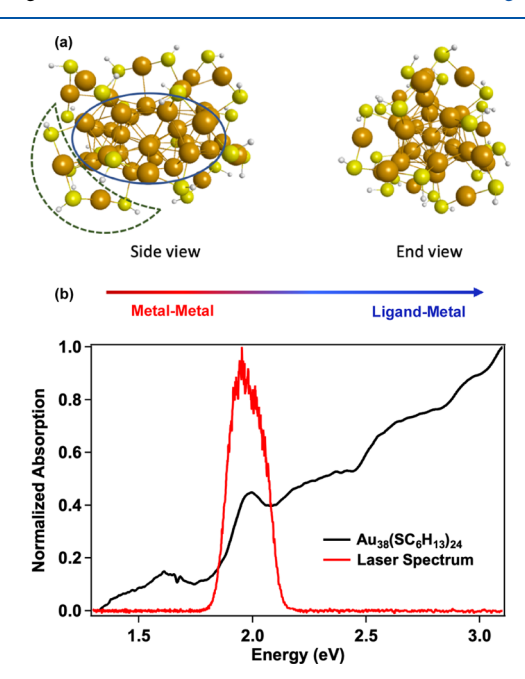


Figure 1. (a) Geometric structure of $\mathrm{Au_{38}(SH)_{24}}$ (Au, gold; S, yellow; and H, white). (b) Normalized absorption of $\mathrm{Au_{38}(SC_6H_{13})_{24}}$ in toluene. Laser spectrum used in p-2DES measurements (red solid line). The top arrow illustrates the generalized transition from mostly metal-centered to mostly ligand-to-metal-centered transitions with increasing energy.

Consideration of the Au-Au kernel and Au-S staples yields a D_3 point group symmetry with the principal C_3 axis parallel to the bi-icosahedral metal kernel.^{20–22} The measured linear absorption spectrum of Au₃₈(SC₆H₁₃)₂₄ dissolved in toluene from this study is shown in Figure 1b and exhibits several absorption bands from 1.4 to 3.1 eV - including the charge transfer resonance centered at ~1.96 eV (~630 nm). The redto-blue arrow in Figure 1b depicts the evolution from predominantly metal-centered to ligand-to-metal charge transfer transitions with increasing excitation energy. For example, TDDFT calculations indicate the lower-energy features from ~1.5 to ~1.8 eV are predominantly composed of transitions between metal-centered LUMO + 1 ← HOMO - 2 orbitals colocalized to the all-metal bi-icosahedral Au_{23} kernel. 20,21 The charge transfer resonance, however, consists of both metalcentered transitions localized in the gold kernel and ligand-tometal transitions of the Au-S semiring unit. 20,21 Generally, transitions in the metal kernel arise from Au 6sp orbitals and the semiring transitions originate from Au 5d and S 3p orbitals. 20,21 As such, TDDFT calculations with SH ligands are expected to result in only small differences between calculated and experimental energies for transitions at near-infrared and visible frequencies.42

Transitions that contribute most significantly to the charge transfer resonance for the calculated $Au_{38}(SH)_{24}$ are provided in Table 1. The laser pulse spectrum in Figure 1b illustrates the

Table 1. Electronic Transitions of Calculated Excited States Covering the 1.9–2.1 eV Range for A₂ and E Symmetry States Determined from TDDFT Calculations on Au₃₈(SH)₂₄ MPCs^a

	energy	oscillator				
state	(eV)	strength	weight	transition		
	A ₂ Symmetry					
S_{19}	1.897	0.028	0.357	HOMO - 8	LUMO	
			0.327	HOMO - 2	LUMO + 2	
			0.041	HOMO - 1	LUMO + 1	
S_{24}	2.013	0.102	0.454	HOMO - 8	LUMO	
			0.094	HOMO - 1	LUMO + 1	
S_{26}	2.093	0.021	0.814	HOMO - 10	LUMO	
			0.132	HOMO - 9	LUMO	
			0.007	HOMO - 1	LUMO + 1	
	E Symmetry					
S_{20}	1.899	0.003	0.827	HOMO - 6	LUMO	
			0.086	HOMO - 2	LUMO + 2	
S_{21}	1.923	0.0002	0.969	HOMO - 7	LUMO	
			0.011	HOMO - 8	LUMO	
S_{22}	1.956	0.002	0.651	HOMO - 8	LUMO	
			0.229	HOMO - 2	LUMO + 2	
S_{23}	1.974	0.028	0.295	HOMO - 8	LUMO	
			0.294	HOMO - 2	LUMO + 2	
			0.142	НОМО	LUMO + 3	
S_{25}	2.085	0.002	0.795	HOMO - 9	LUMO	
S_{27}	2.096	0.001	0.770	HOMO - 10	LUMO	
			0.054	HOMO - 12	LUMO	
			0.101	HOMO - 9	LUMO	

"A full list of states and their contributing transitions are provided in Tables S2 and S3.

resonant excitation range of the p-2DES measurements on the mixed charge transfer resonance. In 2015, Jin et al. characterized a structural isomer of the original Au_{38} cluster, $\mathrm{Au}_{38}\mathrm{Q}.^{43}$ The higher-symmetry isomer, denoted as $\mathrm{Au}_{38}\mathrm{T}$, consists of a 23-gold-atom core but is composed of an Au_{13} icosahedron and an Au_{12} tri-tetrahedron that share two Au atoms. The surface motifs in $\mathrm{Au}_{38}\mathrm{T}$ include three dimeric $\mathrm{Au}_2(\mathrm{SR})_3$, three monomeric $\mathrm{Au}(\mathrm{SR})_2$, two trimeric $\mathrm{Au}_3(\mathrm{SR})_4$ motifs, and one SR bridged staple unit. The two isomers can be distinguished by their distinct electronic absorption spectra. The higher-symmetry $\mathrm{Au}_{38}\mathrm{T}$ isomer does not support a charge transfer resonance at ~ 2.0 eV. Therefore, the observed dynamics in this work are assigned to the $\mathrm{Au}_{38}\mathrm{Q}$ isomer.

Polarization-selective 2DES measurements with copolarized and cross-polarized excitation-detection pulses were used to map the electronic relaxation dynamics of $\mathrm{Au_{38}(SC_6H_{13})_{24}}$ dissolved in toluene. For p-2DES measurements, laser pulses are polarized along one of two orthogonal axes (X or Y) with propagation in the third dimension (Z). Transient signal strengths are monitored using either copolarized (S_{XXXX}) or cross-polarized (S_{XXYY}) excitation and detection fields; the first and second subscripts in S denote the polarization direction of the excitation field and the third and fourth represent the polarization direction of the detection field. Based on the principle of photoselection, the excitation field will prepare an excited state population defined by the pump laser polarization

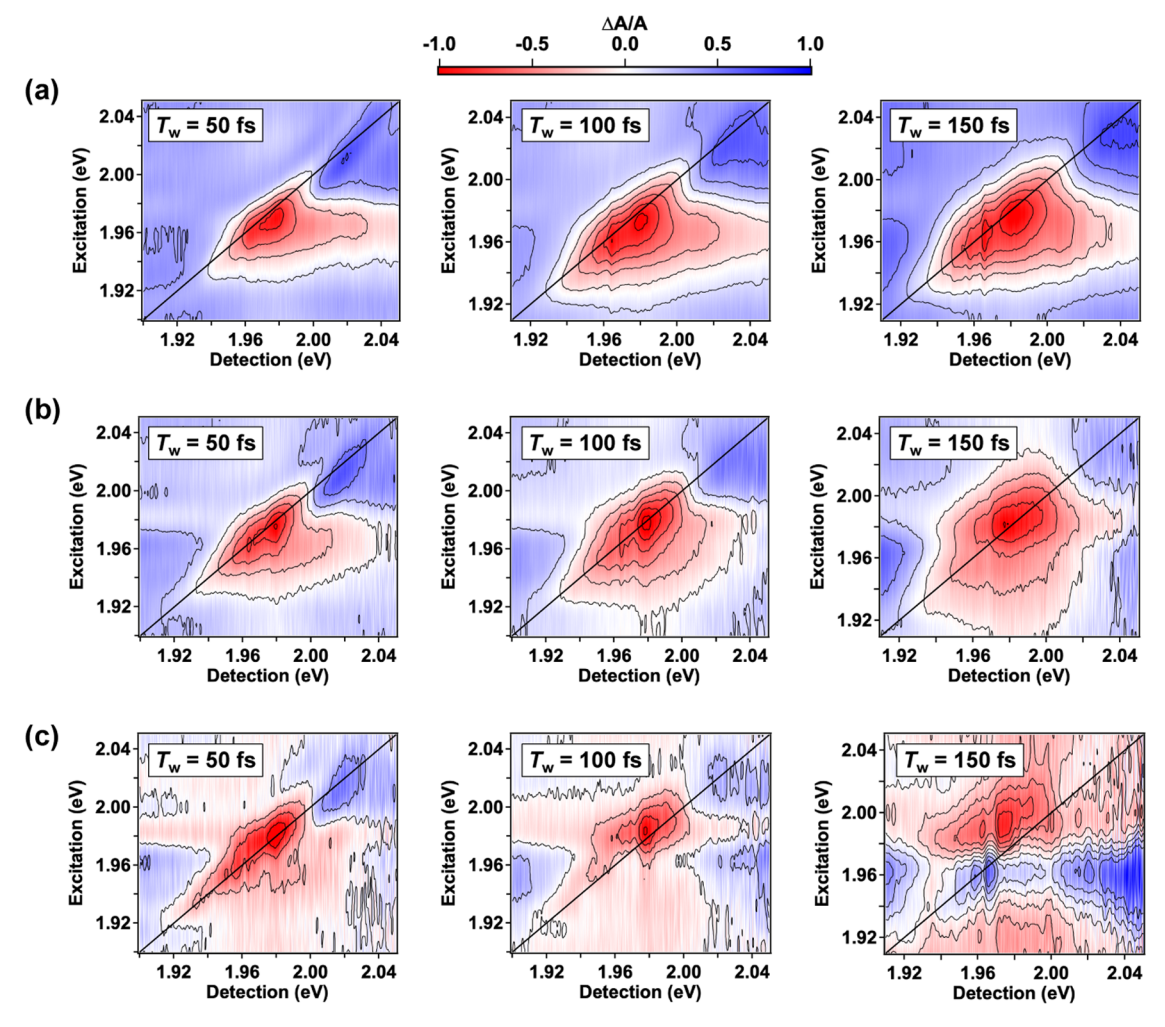


Figure 2. Polarization-dependent absorptive 2DES maps of $Au_{38}(SC_6H_{13})_{24}$ at pump—probe waiting times $T_w = 50$, 100, and 150 fs for (a) copolarized (S_{XXXX}) excitation, (b) cross-polarized (S_{XXXY}) excitation, and (c) cross-peak specific (S_{cp}) maps. S_{cp} maps were determined by scaling the cross-polarized intensity to the copolarized intensity using the expression $S_{cp} = (3 \times S_{XXYY} - S_{XXXX})$. The p-2DES maps are falsely colored such that red and blue colors correspond to negative- and positive-amplitude differential absorption signals, respectively. The 2DES maps in (a, b) were normalized to the maximum transient bleach signal for copolarized and cross-polarized measurements, respectively. The cross-peak specific maps in (c) were determined using the raw intensities for the copolarized and cross-polarized measurements.

plane, and the evolution of this ensemble is monitored by the temporally delayed probe laser. The time-dependent evolution of the excitation-detection frequency correlation from p-2DES measurements on $\mathrm{Au_{38}(SC_6H_{13})_{24}}$ is shown in Figure 2. Figure 2a shows absorptive signals for 2DES maps at pump—probe waiting times $T_{\mathrm{w}}=50$, 100, and 150 fs obtained from copolarized excitation (S_{XXXX}). The absorptive maps are false-colored such that red represents negative and blue represents positive transient amplitude signals. Copolarized excitation results in the formation of multiple bleach components distributed along the diagonal. Strong off-diagonal bleach signals were also detected, correlated to an excitation energy of approx. 1.96 eV.

The spectral weight and relative contributions of the components forming the transient bleach signal evolved as the pump—probe waiting time increased from 50 to 150 fs (Figure 2a). The time dependence of the 2DES spectral profile suggested sequential state-to-state dynamics were responsible for relaxation following electronic excitation of the charge transfer manifold. Polarization-resolved 2DES was used to better understand the transitions that make up the $Au_{38}(SC_6H_{13})_{24}$ transient bleach signals. Figure 2b depicts

the p-2DES maps resulting from cross-polarized (S_{XXYY}) excitation/detection. The data in Figure 2b demonstrate the polarization dependence of the 2DES signal. Both copolarized and cross-polarized p-2DES maps resolved the time-dependent evolution of the multiple peak amplitudes that made up the p-2DES-detected bleach signal. However, the use of crosspolarized excitation/detection schemes resulted in the suppression of the off-diagonal cross-peak measured for 1.96 eV excitation. This observation indicated that among a manifold of electronic charge transfer excitations, transitions with different dipole orientations contributed to energy relaxation in $Au_{38}(SC_6H_{13})_{24}$. In order to distinguish these transitions, we calculated the cross-peak specific spectra (S_{cp}). The cross-peak specific spectra isolate signals originating from transitions with nonparallel dipole moments. 33,38,44cross-peak spectra were determined by scaling the crosspolarized intensity to the copolarized intensity at excitation/ frequency correlations using the expression: $S_{cp} = (3 \times S_{XXYY} S_{XXXX}$). 33,38,44 These spectra enhance low-amplitude signals through suppression of the stronger on-diagonal features and reveal weaker off-diagonal contributions from electronic and vibronic transitions. Cross-peak specific maps at $T_{\rm w}$ = 50, 100,

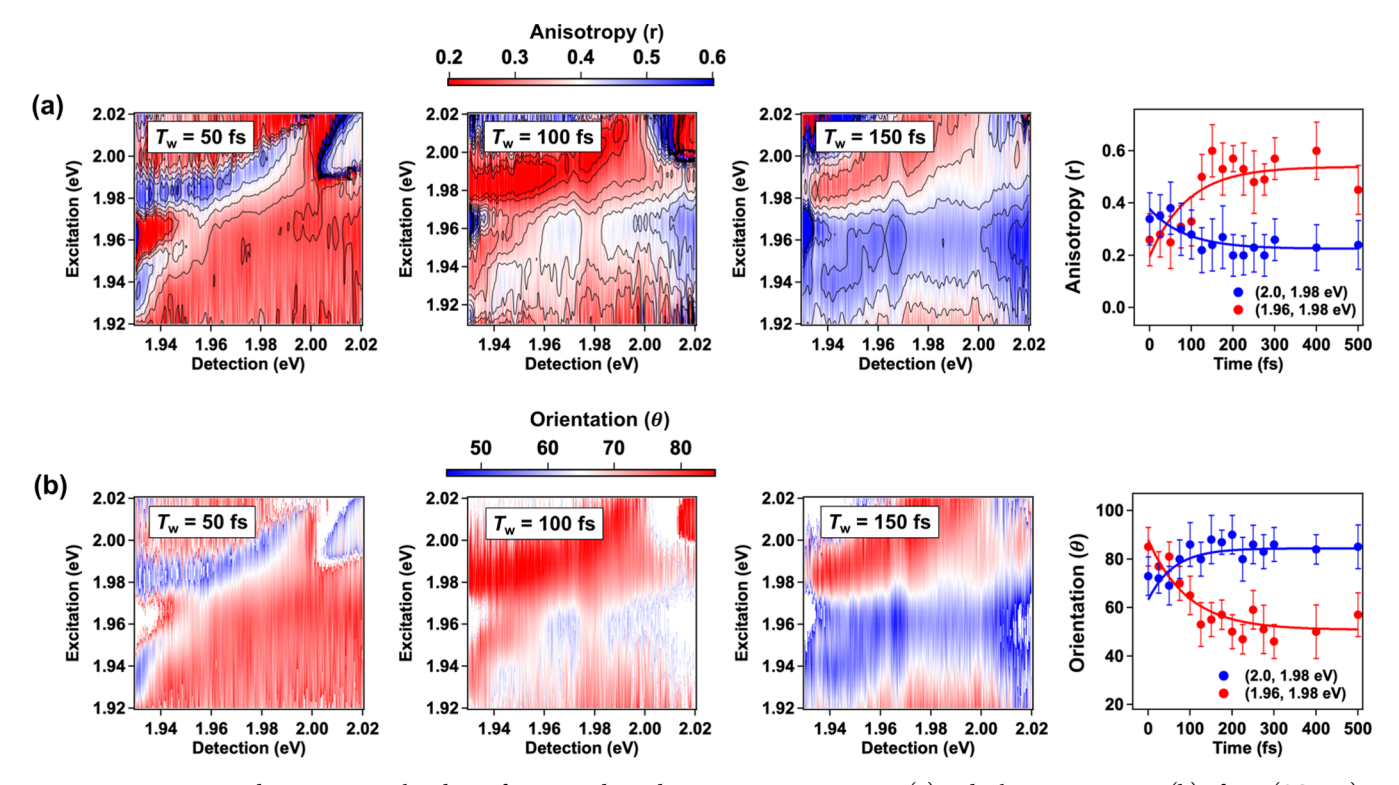


Figure 3. 2D excitation-detection maps that depict frequency-dependent transition anisotropies (a) and relative orientations (b) of $Au_{38}(SC_6H_{13})_{24}$ at pump—probe waiting times $T_w = 50$, 100, and 150 fs. Time-dependent anisotropy and orientation at excitation-detection energies 2.0–1.98 eV (blue) and 1.96–1.98 eV (red) across the T_w range that spans 0–500 fs are included. Maps are false-colored such that red-to-blue corresponds to anisotropies from 0.2 to 0.6 and relative orientations from 80 to 40° , respectively. Time-dependent anisotropies and orientations are fit to single exponentials (solid lines).

and 150 fs are shown in Figure 2c. Comparison of the crosspeak specific maps provides two observations: (1) the timedelayed buildup of a positive differential amplitude signal is resolved at $T_{\rm w}$ = 150 fs, and (2) the positive-amplitude signal is localized to 1.96 eV excitation and spans the detection axis from 1.91 to 2.05 eV. The polarization dependence of the 1.96 eV excitation peak is also demonstrated by comparison of the excitation spectra for the S_{XXXX} , S_{XXYY} , and S_{cp} spectra at T_{w} = 150 fs and are shown in Figure S1. It is also possible to measure cross-peak specific spectra by using pulse polarization combinations like $(60, -60^{\circ}, 0, 0)$ and $(0, 0, 60, -60^{\circ})$, (46,47)where the angles represent the relative electric field polarization of a four-pulse sequence. These polarization schemes suppress on-diagonal peaks and isolate off-diagonal pathways in multidimensional measurements because the emitted thirdorder signal is an intrinsically linear combination of the orientational response. 38,44–48 However, the cross-peak specific spectra can also be obtained through independent measurements of S_{XXXX} and S_{XXYY} polarization schemes and taking the ratio of the signal intensities, as shown by Ogilvie and coworkers.³⁸ This method was implemented here. Qualitatively, the observations in Figure 2c suggest the presence of a specific resonance that has a unique orientation within the spectrally broad charge transfer resonance in $Au_{38}(SC_6H_{13})_{24}$.

To gain further insight into the unique 1.96 eV resonance and characterize the differences between the transitions accessed in the LMCT manifold, the transition anisotropy r and relative transition dipole orientations θ were determined using eqs 1 and 2, respectively.^{38,44}

$$r = \frac{S_{XXXX} - S_{XXYY}}{S_{XXXX} + 2S_{XXYY}} \tag{1}$$

$$\theta = \cos^{-1} \left(\sqrt{\frac{2S_{XXXX} - S_{XXYY}}{S_{XXXX} + 2S_{XXYY}}} \right)$$
 (2)

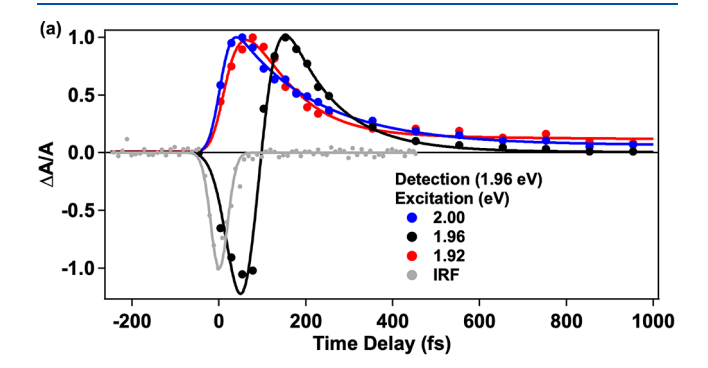
Figure 3a,b shows 2D excitation-detection anisotropy maps that depict the frequency dependence of the transition anisotropy and orientation at $T_{\rm w}$ = 50, 100, and 150 fs, respectively. The time-dependent anisotropies and orientations at excitation-detection energies 2.0-1.98 and 1.96-1.98 eV from $T_{\rm w}$ = 0-500 fs are included. Similar to the $S_{\rm cp}$ maps in Figure 2c that show a positive differential amplitude signal localized to 1.96 eV excitation, the 2D excitation-detection anisotropy maps show a narrow band anisotropy region that is superimposed on top of a broad manifold of similar anisotropies. At $T_{\rm w}$ = 150 fs and excitation at 1.96 eV, r = 0.55, and $\theta = 50^{\circ}$, which are distinct from transitions excited above and below 1.96 eV (r = 0.25 and $\theta = 80^{\circ}$). However, the narrow anisotropy and orientation region at 1.96 eV exhibited a time-dependent buildup that was quantified by fitting the time-resolved anisotropy and orientation at 1.96-1.98 eV using $T_{\rm w}$ values spanning from 0 to 500 fs. A single-exponential fit yielded a growth time constant of 90 \pm 40 and 80 \pm 40 fs for the anisotropy and orientation, respectively. Both the anisotropy and orientation at 2.0-1.98 eV showed a slight buildup of 70 \pm 40 fs. Figure S2 shows the anisotropy and orientation values spanning the range from $T_{\rm w}$ = 0 to 2500 fs. No statistically significant change occurred beyond the initial buildup. It is also possible for PIA, GSB, and stimulated emission (SE) pathways to interfere with orientation and

anisotropy calculations. 44,48 Within the Franck-Condon approximation, SE and GSB signals will have the same anisotropy after internal conversion (~100 fs), which is observed at excitation 1.96 and 2.0 eV in Figure 3a. A similar observation was observed in p-2DES measurements on photosynthetic pigments.³⁸ Population transfer can also alter anisotropy determinations. 33,44 In this case, the measured value likely corresponds to the new mode. The time-dependent anisotropy shown in Figure 3a suggests that population transfer is, in part, responsible for the change in anisotropy at 1.96 eV excitation. These results indicate that p-2DES could be effectively used to distinguish electronic transitions that originated from different intermediate states that had distinctive transient anisotropies and dipole orientations. In particular, a transition at 1.96 eV was distinguished from the manifold of transitions that comprised the LMCT resonance in $Au_{38}(SC_6H_{13})_{24}$.

Next, the experimental results are discussed in the context of computational predictions for the electronic transitions. These states have predicted oscillator strengths and spectral weights that can be used to assign the states that contribute to the LMCT resonance. TDDFT calculations also include specific orbital symmetries that can be used to infer the structural origin of specific transitions. As listed in Table 1, the dominant state in the 1.9–2.1 eV range (S_{24}) arises from the LUMO \leftarrow HOMO - 8 transition; the LUMO + 1 \leftarrow HOMO - 1 transition also contributes significantly to the transition dipole moment and thus to the oscillator strength (Table S2). The LUMO \leftarrow HOMO - 8 transition arises from excitation out of an a_2 -type symmetry orbital localized to the inorganic semiring into a degenerate set of Au 6sp orbitals primarily localized in the metal kernel. The E states in this energy range have a dominant contribution from the LUMO + $2 \leftarrow HOMO - 2$ transition, which arises from Au 6sp orbitals localized to the metal kernel, in addition to transitions from semiring-based orbitals into the LUMO. Unique to E states, the LUMO ← HOMO - 7 transition (S_{21}) originates almost entirely from excitations out of the semiring orbitals; the HOMO - 7 is composed of S 3p and Au 5d orbitals, with some Au 6sp character. For molecular D_3 point group symmetry, selection rules indicate that this transition is allowed for X- and Ypolarized light and would likely still contribute to the crosspeak specific spectra from p-2DES measurements. Because S₂₁ has a relatively low oscillator strength compared to other states, it would likely have low amplitude compared to the stronger contributions from bright states in a traditional 2DES measurement that employs copolarized excitation fields. Here, the use of p-2DES helps to resolve this transition by the suppression of the strong on-diagonal signals of the so-called bright states. Given the low oscillator strength of S_{21} , this could be an effectively dark state that is indirectly populated through relaxation of the bright A_2 states, such as S_{24} , following photoexcitation. Therefore, on the basis of calculated state symmetries and experimental frequency-dependent anisotropies and orientations from p-2DES, we currently assign the transient intermediate state accessed by 1.96 eV excitation to the LUMO \leftarrow HOMO - 7 transition. The results highlight the importance of orbital symmetry, and not just brightness of a given excited state, in determining the photoexcitation and relaxation dynamics in $Au_{38}(SC_6H_{13})_{24}$.

Given that the positive differential amplitude signal is detected in only a narrow excitation energy range, centered at 1.96 eV, and has unique anisotropy and orientation values with

respect to the rest of the excitation bandwidth, the time-dependent amplitudes of the 2DES-detected cross-peaks (from $S_{\rm cp}$ spectra) were analyzed to understand the dynamics of the E-symmetry species. The time-dependent amplitudes measured at 1.98 eV detection were compared for three different excitation energies: 2.0, 1.96, and 1.92 eV (Figure 4a). Each



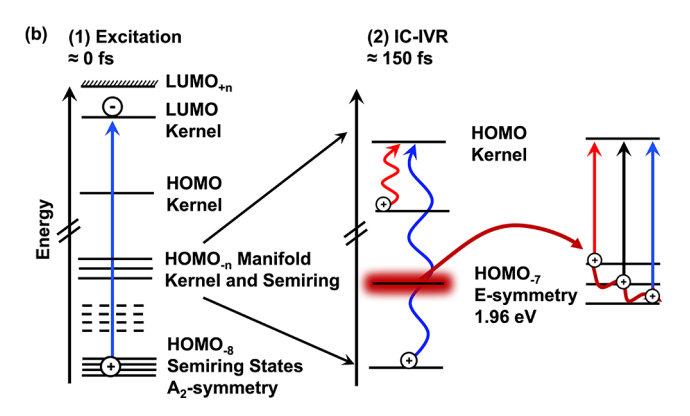


Figure 4. Detection energy dependence of the time-dependent amplitudes of p-2DES-detected cross-peaks from the S_{cp} spectra at three different excitation energies: (a) 2.0 1.96, and 1.92 eV. The pump—probe time delay range is -250 to 1000 fs. Each trace was fit to exponentials convoluted with the instrument response that used a least-squares analysis (solid lines). Each trace was normalized to the time delay with maximum amplitude throughout the pump—probe delay series. The IRF is overlaid in gray. (b) Schematic depicting the ultrafast (sub-500 fs) electronic charge carrier relaxation mechanism following excitation of the charge transfer resonance at \sim 2.0 eV in $Au_{38}(SC_6H_{13})_{24}$.

trace was normalized to its maximum amplitude across the pump-probe time delay and fit to a multicomponent kinetic model that includes kinetic time constants, amplitudes, and convolution of the experimental instrument response. The time-dependent $S_{\rm cp}$ amplitudes and corresponding fits are shown in Figure 4a. Excitation using 2.0 and 1.92 eV yielded similar time-dependent profiles, which included a nearinstantaneous buildup of signal within the instrument response time of 40 \pm 5 fs, and fast decay time constants of 175 \pm 45 and 200 \pm 40 fs, respectively. The time dependence of the $S_{\rm cp}$ data obtained for 1.96 eV excitation was distinct from all other sampled energies. Figure 4a shows a clear derivative line shape that suggests the positive differential amplitude signature does not occur instantaneously but rather is generated after the initially excited carriers have relaxed through an intermediate pathway within \sim 150 fs. Furthermore, the 110 \pm 40 fs decay time constant of the positive differential amplitude feature is accelerated compared to those measured for 2.0 and 1.92 eV

excitation. These time-domain responses, which are unique to 1.96 eV excitation, suggest the E-symmetry species of the semiring exhibits dynamics that are distinguishable from the majority of the LMCT excitation manifold. Based on the timedependent buildup of the 1.96 eV positive differential amplitude signal, this transition likely corresponds to a dark state or weak transition (such as S_{21} from Table 1) that is indirectly populated through relaxation from the initially excited bright states of the LMCT manifold. The detection energy dependence of the relaxation rate constants at 2.0, 1.96, and 1.92 eV excitation all showed a monotonic decrease with increasing detection energy (Figures S3 and S4), which is consistent with predictions based on well-known energy-gap laws.49 However, the overall accelerated relaxation rate constants of the positive differential amplitude signature at 1.96 eV with respect to all other excitation energies employed suggest that carriers mediated by the S₂₁ state may relax through different channels than the rest of the electronic manifold.

A mechanism that depicts electronic charge carrier relaxation through a manifold of intermediate states in $Au_{38}(SC_6H_{13})_{24}$ is presented in Figure 4b. Photoexcitation populates several of the inorganic semiring and metal kernel states. However, initial absorption is likely dominated by the bright A_2 states via the LUMO \leftarrow HOMO - 8 semiring transition. The excited hole carriers relax through internal conversion into the mixed metal kernel and an inorganic semiring LUMO \leftarrow HOMO - n manifold that includes the semiring-localized LUMO ← HOMO − 7 transition with E symmetry. Within the mixed metal and semiring manifold, the charge carriers initially prepared by 1.96 eV excitation thermalize through a unique relaxation channel mediated by the HOMO - 7 semiring orbitals. The physical picture that emerges is that although a broad manifold of LMCT resonances are populated, 1.96 eV excitation accesses different regions of the potential surface and indirectly populates semiring HOMO - 7 orbitals leading to a weak E-symmetry state (S_{21}) that thermalizes within the electronic manifold. Two explanations for this state specificity in electronic relaxation dynamics could be internal conversion between bright and dark E states with nonequivalent symmetry (e.g., nonequivalent subgroups of a higher-symmetry point group) or internal conversion between states with different degrees of contributions from kernel-kernel and kernel-semiring excitations (e.g., due to differences in coupling of the semiringlocalized LUMO ← HOMO - 7 transition vs the semiringlocalized LUMO ← HOMO − 8 transition with the kernelbased LUMO + 2 \leftarrow HOMO - 2 transition, which is a component of multiple states in this energy region). Although the current data cannot distinguish these cases, the importance of state specificity in electronic relaxation dynamics for Au₃₈(SC₆H₁₃)₂₄ is clearly evident. The observation of statesymmetry-specific dynamics for Au₃₈(SC₆H₁₃)₂₄ is surprising, given the high density of states of this colloidal metal nanocluster. These results provide new fundamental insights on symmetry-dependent relaxation dynamics in Au₃₈(SC₆H₁₃)₂₄, which suggest structural modifications to the metal kernel and inorganic semiring structures could influence the flow of energy in photoexcited nanoclusters.

CONCLUSIONS

In conclusion, the influence of excited state symmetry on electronic carrier relaxation was studied in the $Au_{38}(SC_6H_{13})_{24}$

MPC. These insights were made possible by the use of polarization-selective 2DES, which resolved cross-peaks attributed to a dark semiring state. Characterization of p-2DES spectra identified distinct dynamics, anisotropy, and excited state transition dipole orientations for states accessed by 1.96 eV excitation. Comparison of the p-2DES data to electronic state descriptions from TDDFT calculations and consideration of spectroscopic selection rules indicated that the e-type symmetry orbitals of the LUMO \leftarrow HOMO - 7 are indirectly populated, which occurs because of a transition out of the HOMO - 7 orbital localized to the $Au_{38}(SC_6H_{13})_{24}$ semiring into the degenerate LUMO that is primarily localized in the metal kernel. This suggested that state-specific symmetries that comprise the LMCT manifold govern relaxation dynamics in metal clusters, despite the near degeneracy with a high density of other electronic states. This example of state selectivity in the relaxation dynamics is reminiscent of molecular systems and highlights the important role of state-to-state interactions in atomically precise gold nanoclusters. Analysis of time-dependent amplitudes of p-2DES-detected cross-peaks resolved a time-delayed buildup of a positive differential amplitude signal generated by 1.96 eV excitation. This indicated that the 1.96 eV transition is likely coupled to a dark E-symmetry state that is indirectly populated through relaxation from the initially excited A2 states arising from excitations out of the orbitals localized to the inorganic semiring. The results demonstrate the effectiveness of p-2DES for dissecting the complex dynamics in colloidal nanoclusters. The observation of symmetry-dependent dynamics shows promise for the use of targeted synthetic modifications to control energy flow in sub- to few-nanometer metal nanoclusters.

ASSOCIATED CONTENT

Supporting Information

The Supporting Information is available free of charge at https://pubs.acs.org/doi/10.1021/acs.jpcc.3c04832.

Details of computational methods for TDDFT calculations; frontier orbital information; transitions responsible for the lowest-energy A_2 and E states, and additional polarization-selective 2DES data (PDF)

AUTHOR INFORMATION

Corresponding Authors

Christine M. Aikens — Department of Chemistry, Kansas State University, Manhattan, Kansas 66506, United States; orcid.org/0000-0002-0854-7997; Email: cmaikens@ksu.edu

Kenneth L. Knappenberger, Jr. – Department of Chemistry, The Pennsylvania State University, University Park, Pennsylvania 16802, United States; oorcid.org/0000-0003-4123-3663; Email: klk260@psu.edu

Autho

William R. Jeffries — Department of Chemistry, The Pennsylvania State University, University Park, Pennsylvania 16802, United States; orcid.org/0000-0002-4870-5910

Complete contact information is available at: https://pubs.acs.org/10.1021/acs.jpcc.3c04832

Notes

The authors declare no competing financial interest.

ACKNOWLEDGMENTS

This research was supported by a grant from the Air Force Office of Scientific Research, grant number (FA9550-22-1-0402). W.R.J. was supported by awards from the National Science Foundation (CHE-1904876 and CHE-2204190). C.M.A. was supported by the National Science Foundation (CHE-1905048). The authors gratefully acknowledge Dr. Stefan Knoppe for providing the Au₃₈ metal nanoclusters used for this experiment.

REFERENCES

- (1) Hartland, G. V. Optical Studies of Dynamics in Noble Metal Nanostructures. *Chem. Rev.* **2011**, *111*, 3858–3887.
- (2) Arbouet, A.; Voisin, C.; Christofilos, D.; Langot, P.; Fatti, N. D.; Vallée, F.; Lermé, J.; Celep, G.; Cottancin, E.; Gaudry, M.; et al. Electron-Phonon Scattering in Metal Clusters. *Phys. Rev. Lett.* **2003**, 90, No. 177401.
- (3) Green, T. D.; Knappenberger, K. L., Jr. Relaxation dynamics of $\mathrm{Au}_{25}\mathrm{L}_{18}$ nanoclusters studied by femtosecond time-resolved near infrared transient absorption spectroscopy. *Nanoscale* **2012**, *4*, 4111–4118
- (4) Miller, S. A.; Womick, J. M.; Parker, J. F.; Murray, R. W.; Moran, A. M. Femtosecond Relaxation Dynamics of Au₂₅L₁₈⁻ Monolayer-Protected Clusters. *J. Phys. Chem. C* **2009**, *113*, 9440–9444.
- (5) Zhao, T.; Herbert, P. J.; Zheng, H.; Knappenberger, K. L., Jr. State-Resolved Metal Nanoparticle Dynamics Viewed through the Combined Lenses of Ultrafast and Magneto-optical Spectroscopies. *Acc. Chem. Res.* 2018, *51*, 1433–1442.
- (6) Jeffries, W. R.; Wallace, J.; Knappenberger, K. L., Jr. Ultrafast Relaxation Dynamics of Au₃₈(SC₆H₁₃)₂₄ Monolayer-Protected Clusters Resolved by Two-Dimensional Electronic Spectroscopy. *J. Chem. Phys.* **2021**, *155*, No. 124303.
- (7) Stoll, T.; Sgro, E.; Jarrett, J. W.; Rehault, J.; Oriana, A.; Sala, L.; Branchi, F.; Cerullo, G.; Knappenberger, K. L., Jr. Superatom State-Resolved Dynamics of the Au₂₅(SC₈H₉)₁₈ Cluster from Two-Dimensional Electronic Spectroscopy. *J. Am. Chem. Soc.* **2016**, *138*, 1788–1791.
- (8) Zhou, M.; Tian, S.; Zeng, C.; Sfeir, M. Y.; Wu, Z.; Jin, R. Ultrafast Relaxation Dynamics of Au₃₈(SC₂H₄Ph)₂₄ Nanoclusters and Effects of Structural Isomerism. *J. Phys. Chem. C* **2017**, *121*, 10686–10693.
- (9) Jadzinsky, P. D.; Calero, G.; Ackerson, C. J.; Bushnell, D. A.; Kornberg, R. D. Structure of a Thiol Monolayer-Protected Gold Nanoparticle at 1.1 Å Resolution. *Science* **2007**, *318*, 430–433.
- (10) Heaven, M. W.; Dass, A.; White, P. S.; Holt, K. M.; Murray, R. W. Crystal Structure of the Gold Nanoparticle $[N(C_8H_{17})_4]$ - $[Au_{25}(SCH_2CH_2Ph_{18})]$. J. Am. Chem. Soc. **2008**, 130, 3754–3755.
- (11) Herbert, P. J.; Knappenberger, K. L., Jr. Spin-Polarized Photoluminescence in Au₂₅(SC₈H₉)₁₈ Monolayer-Protected Clusters. *Small* **2021**, *17*, No. 2004431.
- (12) Herbert, P. J.; Tofanelli, M. A.; Ackerson, C. J.; Knappenberger, K. L., Jr. The Influence of Pd-Atom Substitution on $\mathrm{Au}_{25}(\mathrm{SC_8H_9})_{18}$ Cluster Photoluminescence. *J. Phys. Chem. C* **2021**, *125*, 7267–7275.
- (13) Herbert, P. J.; Ackerson, C. J.; Knappenberger, K. L., Jr. Size-Scalable Near-Infrared Photoluminescence in Gold Monolayer Protected Clusters. *J. Phys. Chem. Lett.* **2021**, *12*, 7531–7536.
- (14) Castleman, A. W.; Bowen, K. H. Clusters: Structure, Energetics, and Dynamics of Intermediate States of Matter. *J. Phys. Chem. A* **1996**, *100*, 12911–12944.
- (15) Valden, M.; Lai, X.; Goodman, D. W. Onset of Catalytic Activity of Gold Clusters on Titania with the Appearance of Nonmetallic Properties. *Science* **1998**, 281, 1647–1650.
- (16) Yoon, B.; Häkkinen, H.; Landman, U. Interaction of O₂ with Gold Clusters: Molecular and Dissociative Adsorption. *J. Phys. Chem.* A **2003**, *107*, 4066–4071.

- (17) Lopez-Acevedo, O.; Kacprzak, K. A.; Akola, J.; Häkkinen, H. Quantum Size Effects in Ambient CO Oxidation Catalysed by Ligand-Protected Gold Clusters. *Nat. Chem.* **2010**, *2*, 329–334.
- (18) Zhao, J.; Li, Q.; Zhuang, S.; Song, Y.; Morris, D. J.; Zhou, M.; Wu, Z.; Zhang, P.; Jin, R. Reversible Control of Chemoselectivity in Au₃₈(SR)₂₄ Nanocluster-Catalyzed Transfer Hydrogenation in Nitrobenzaldehyde Derivatives. *J. Phys. Chem. Lett.* **2018**, *9*, 7173–7179.
- (19) Pei, Y.; Gai, Y.; Zeng, C. Structural Prediction of Thiolate-Protected Au_{38} : A Face-Fused Bi-icosahedral Au Core. *J. Am. Chem. Soc.* **2008**, *130*, 7830–7832.
- (20) Lopez-Acevedo, O.; Tsunoyama, H.; Tsukuda, T.; Häkkinen, H.; Aikens, C. M. Chirality and Electronic Structure of the Thiolate-Protected Au₃₈ Nanocluster. *J. Am. Chem. Soc.* **2010**, *132*, 8210–8218.
- (21) Senanayake, R. D.; Guidez, E. B.; Neukirch, A. J.; Prezhdo, O. V.; Aikens, C. M. Theoretical Investigation of Relaxation Dynamics in Au₃₈(SH)₂₄ Thiolate-Protected Gold Nanoclusters. *J. Phys. Chem. C* **2018**, *122*, 16380–16388.
- (22) Qian, H.; Eckenhoff, W. T.; Zhu, Y.; Pintauer, T.; Jin, R. Total Structure Determination of Thiolate-Protected Au₃₈ Nanoparticles. *J. Am. Chem. Soc.* **2010**, *132*, 8280–8281.
- (23) Brixner, T.; Stenger, J.; Vaswani, H. M.; Cho, M.; Blankenship, R. E.; Fleming, G. R. Two-Dimensional Spectroscopy of Electronic Couplings in Photosynthesis. *Nature* **2005**, *434*, 625–628.
- (24) Myers, J. A.; Lewis, K. L. M.; Fuller, F. D.; Tekavec, P. F.; Yocum, C. F.; Ogilvie, J. P. Two-Dimensional Electronic Spectroscopy of the D1-D2-cyt b559 Photosystem II Reaction Center Complex. J. Phys. Chem. Lett. 2010, 1, 2774–2780.
- (25) Nemeth, A.; Milota, F.; Mančal, T.; Lukeš, V.; Kauffmann, H. F.; Sperling, J. Vibronic Modulation of Lineshapes in Two-Dimensional Electronic Spectra. *Chem. Phys. Lett.* **2008**, 459, 94–99. (26) Mančal, T.; Christensson, N.; Lukeš, V.; Milota, F.; Brixner, O.;
- Kauffmann, H. F.; Hauer, J. System-Dependent Signatures of Electronic and Vibrational Coherences in Electronic Two-Dimensional Spectroscopy. *J. Phys. Chem. Lett.* **2012**, *3*, 1497–1502.
- (27) Turner, D. B.; Hassan, Y.; Scholes, G. D. Exciton Superposition States in CdSe Nanocrystals Measured Using Broadband Two-Dimensional Electronic Spectroscopy. *Nano Lett.* **2012**, *12*, 880–886. (28) Wood, R. E.; Lloyd, L. T.; Mujid, F.; Wang, L.; Allodi, M. A.; Gao, H.; Mazuski, R.; Ting, P. C.; Xie, S.; Park, J.; Engel, G. S. Evidence for the Dominance of Carrier-Induced Bandgap Renormalization Over Biexciton Formation in Cryogenic Ultrafast Experiments on MoS₂ Monolayers. *J. Phys. Chem. Lett.* **2020**, *11*, 2658–2666
- (29) Jarrett, J. W.; Yi, C.; Stoll, T.; Rehault, J.; Oriana, A.; Branchi, F.; Cerullo, G.; Knappenberger, K. L., Jr. Dissecting Charge Relaxation Pathways in CdSe/CdS Nanocrystals Using Femtosecond Two-Dimensional Electronic Spectroscopy. *Nanoscale* **2017**, *9*, 4572–4577.
- (30) Policht, V. R.; Russo, M.; Liu, F.; Trovatello, C.; Maiuri, M.; Bai, Y.; Zhu, X.; Conte, S. D.; Cerullo, G. Dissecting Interlayer Hole and Electron Transfer in Transition Metal Dichalcogenide Heterostructures via Two-Dimensional Electronic Spectroscopy. *Nano Lett.* **2021**, *21*, 4738–4743.
- (31) Faeder, S. M. G.; Jonas, D. M. Two-Dimensional Electronic Correlation and Relaxation Spectra: Theory and Model Calculations. *J. Phys. Chem. A* **1999**, *103*, 10489–10505.
- (32) Hybl, J. D.; Albrecht, A. A.; Jonas, D. M. Two-dimensional Fourier Transform Electronic Spectroscopy. *J. Chem. Phys.* **2001**, *115*, 6606–6622.
- (33) Hochstrasser, R. M. Two-Dimensional IR-Spectroscopy: Polarization Anisotropy Effects. *Chem. Phys.* **2001**, *266*, 273–284.
- (34) Wong, C. Y.; Scholes, G. D. Biexcitonic Fine Structure of CdSe Nanocrystals Probed by Polarization-Dependent Two-Dimensional Photon Echo Spectroscopy. *J. Phys. Chem. A* **2011**, *115*, 3797–3806.
- (35) Zhang, T.; Kuznetsova, I.; Meier, T.; Li, X.; Mirin, R. P.; Thomas, P.; Cundiff, S. T. Polarization-Dependent Optical 2D Fourier Transform Spectroscopy of Semiconductors. *Proc. Natl. Acad. Sci. U.S.A.* 2007, 104, 14227–14232.

- (36) Mehlenbacher, R. D.; Wang, J.; Kearns, N. M.; Shea, M. J.; Flach, J. T.; McDonough, T. J.; Wi, M. Y.; Arnold, M. S.; Zanni, M. T. Ultrafast Exciton Hopping Observed in Bare Semiconducting Carbon Nanotube Thin Films with Two-Dimensional White-Light Spectroscopy. J. Phys. Chem. Lett. 2016, 7, 2024–2031.
- (37) Thyrhaug, E.; Zidek, K.; Dostal, J.; Bina, D.; Zigmantas, D. Exciton Structure and Energy Transfer in the Fenna-Matthews-Olsen Complex. J. Phys. Chem. Lett. **2016**, *7*, 1653–1660.
- (38) Song, Y.; Schubert, A.; Maret, E.; Burdick, R. K.; Dunietz, B. D.; Geva, E.; Ogilvie, J. P. Vibronic Structure of Photosynthetic Pigments Probed by Polarized Two-Dimensional Electronic Spectroscopy and *ab initio* Calculations. *Chem. Sci.* **2019**, *10*, 8143–8153.
- (39) Knoppe, S.; Dharmaratne, A. C.; Schreiner, E.; Dass, A.; Burgi, T. Ligand Exchange Reactions on Au₃₈ and Au₄₀ Clusters: A Combined Circular Dichroism and Mass Spectrometry Study. *J. Am. Chem. Soc.* **2010**, *132*, 16783–16789.
- (40) Jeffries, W. R.; Park, K.; Vaia, R. A.; Knappenberger, K. L., Jr. Resolving Electron–Electron Scattering in Plasmonic Nanorod Ensembles Using Two-Dimensional Electronic Spectroscopy. *Nano Lett.* **2020**, 20, 7722–7727.
- (41) Steves, M. A.; Zheng, H.; Knappenberger, K. L., Jr. Correlated Spatially Resolved Two-Dimensional Electronic and Linear Absorption Spectroscopy. *Opt. Lett.* **2019**, *44*, 2117–2120.
- (42) Aikens, C. M. Electronic Structure of Ligand-Passivated Gold and Silver Nanoclusters. J. Phys. Chem. Lett. 2011, 2, 99–104.
- (43) Tian, S.; Li, Y. Z.; Li, M. B.; Yuan, J.; Yang, J.; Wu, Z.; Jin, R. Structural Isomerism in Gold Nanoparticles Revealed by X-ray Crystallography. *Nat. Commun.* **2015**, *6*, No. 8667.
- (44) Hamm, P.; Zanni, M. Concepts and Methods of 2D Infrared Spectroscopy; Cambridge University Press: Cambridge, 2011.
- (45) Read, E. L.; Engel, G. S.; Calhoun, T. R.; Mancal, T.; Ahn-Tae, K.; Blankenship, R. E.; Fleming, G. R. Cross-Peak-Specific Two-Dimensional Electronic Spectroscopy. *Proc. Natl. Acad. Sci. U.S.A.* **2007**, *104*, 14203–14208.
- (46) Zanni, M. T.; Ge, N.-H.; Kim, Y. S.; Hochstrasser, R. M. Two-Dimensional IR Spectroscopy can be Designed to Eliminate the Diagonal Peaks and Expose Only the Crosspeaks Needed for Structure Determination. *Proc. Natl. Acad. Sci. U.S.A.* **2001**, 98, 11265–11270.
- (47) Farrell, K. M.; Yang, N.; Zanni, M. T. A Polarization Scheme that Resolves Cross-Peaks with Transient Absorption and Eliminates Diagonal Peaks in 2D Spectroscopy. *Proc. Natl. Acad. Sci. U.S.A.* **2022**, *119*, No. e2117398119.
- (48) Qian, W.; Jonas, D. M. Role of Cyclic Sets of Transition Dipoles in the Pump—Probe Polarization Anisotropy: Application to Square Symmetric Molecules and Perpendicular Chomophore Pairs. *J. Chem. Phys.* **2003**, *119*, 1611–1622.
- (49) Freed, K. F.; Jortner, J. Multiphonon Processes in the Nonradiative Decay of Large Molecules. *J. Chem. Phys.* **1970**, *52*, 6272–6291.